ADVANCED FUNCTIONAL MATERIALS
www.afm-journal.de

Influence of Electron Acceptor and Electron Donor on the Photophysical Properties of Carbon Dots: A Comparative Investigation at the Bulk-State and Single-Particle Level

Indrajit Srivastava, John S. Khamo, Subhendu Pandit, Parinaz Fathi, Xuedong Huang, Anleen Cao, Richard T. Haasch, Shuming Nie, Kai Zhang, and Dipanjan Pan**

Carbon dots (CDs) are extensively studied to investigate their unique optical properties such as undergoing electron transfer in different scenarios. This work presents an in-depth investigation to study the ensemble-averaged state/bulk state and single-particle level photophysical properties of CDs that are passivated with electron-accepting (CD-A) and electron-donating molecules (CD-D) on their surface. The bulk-state experiments reveal that in a mixture of these CDs, CD-A dominates the overall photophyiscal properties and eventually leads to formation of at least two associated geometries, which is dependent on time, concentration, intramolecular electron/charge transfer, and hydrogen bonding. Single-particle studies, however, do not reveal an "acceptor-dominating" scenario based on analysis of instantaneous intensity, bleaching kinetics, and photoblinking, indicating that the direct interaction of these CDs may affect their photophysical properties in the bulk state due to formation of hierarchical structural assemblies. Here it is anticipated that these fundamental results will further provide insights toward the understanding of the complex mechanism associated with CD emission, which is one of the key contributors to their successful application. As an immediate application of these functional CDs, it is shown that they can be used as a sensing array for metal ions and serve as a powerful toolbox for their technological applications.

1. Introduction

Carbon dots (CDs) have emerged as a promising class of nanomaterials that have widespread applications in optical sensing, photocatalysis, photovoltaic applications, and bioimaging.[1–15] These nanodots have a multitude of intriguing advantages, such as their water solubility, low toxicity, high biocompatibility, easy synthesis techniques, and complementary energy and charge transfer properties.[16–25] However, despite considerable efforts, many questions remain about the intrinsic mechanisms governing their photoluminescence (PL) and its subsequent capability to participate in photoinduced charge-transfer processes.[26,27]

For charge-transfer processes, having a precise control over the interactions between the two components is of prime importance.[28] One way could be by using a suitable precursor for synthesis allowing the CD surface to have a variety of functional groups as desired, such as carboxyl, hydroxyl, amines, etc., which could further allow electron donors and acceptors to be assembled by means of covalent bridges leading to a spatial control over the arrangement. Alternatively, hydrogen bonding could also be utilized owing to it being more directional when compared to other noncovalent bonding interactions, such as electrostatics or π-stacking.[29–32]

I. Srivastava, P. Fathi, Prof. S. Nie, Prof. D. Pan
Departments of Bioengineering
University of Illinois at Urbana-Champaign
Urbana, IL 61801, USA
E-mail: dipanjan@illinois.edu

I. Srivastava, P. Fathi, Prof. S. Nie, Prof. D. Pan
Beckman Institute
University of Illinois at Urbana-Champaign
Urbana, IL 61801, USA

I. Srivastava, S. Pandit, P. Fathi, A. Cao, Prof. S. Nie, Prof. D. Pan
Mills Breast Cancer Institute
Carle Foundation Hospital
Urbana, IL 61801, USA

The ORCID identification number(s) for the author(s) of this article can be found under https://doi.org/10.1002/adfm.201902466.

DOI: 10.1002/adfm.201902466

J. S. Khamo, Prof. K. Zhang
Department of Biochemistry
University of Illinois at Urbana-Champaign
Urbana, IL 61801, USA
E-mail: kaizkaiz@illinois.edu

S. Pandit, Prof. S. Nie
Department of Chemistry
University of Illinois at Urbana-Champaign
Urbana, IL 61801, USA

X. Huang
Department of Chemistry
Fudan University
Shanghai 200433, P. R. China

Dr. R. T. Haasch
Frederick Seitz Materials Research Laboratory Central Research Facilities
University of Illinois at Urbana-Champaign
Urbana, IL 61801, USA

Over the last few years, several researchers have shown that CDs conjugated with different molecules, such as porphyrins, perylenediimides, and extended tetrathiafulvalene (exTTF), participate in photoinduced charge-transfer processes.[33–36] They confirm that CDs can act as either electron donors or electron acceptors due to their bivalent redox character, which indirectly means that upon photoirradiation, CDs can donate their electron when conjugated with perylenediimides[34] and accept electrons when conjugated with porphyrins or exTTF.[35,36] Recently, Vallan et al. have shown that when exfoliated semiconducting metal dichalcogenides such as MoS_2 and WS_2 are chemically conjugated with CDs, they can participate in a charge-transfer process.[37] These studies are of paramount importance in pointing out the role of CDs as a building block for designing photoactive hybrids for optoelectronic devices. However, to the best of our knowledge, most of the studies conducted on studying the given nature of CDs have been conducted at the bulk level and have not been correlated with their photophysical properties at the single-particle level. This comparative information could be critical because CDs have shown excitation-dependent emission shifts associated with ensemble emission spectroscopic studies suggesting that they may possess multi-chromophoric units, which could be attributed to different chemical groups on the nanoscale surface.[38–40] However, there are still misgivings as to whether multiple emission species exists on a single CD or multiple CDs. Furthermore, phenomena such as fluorescence blinking and photostability get concealed in fluorescence emission studies due to inhomogeneity in size, shape, and chemical defects. Consequently, a more in-depth understanding of the correlation of acceptor or donor molecules on the photophysical properties and intrinsic fluorescence mechanisms of CDs both at bulk level or single-particle level would be highly beneficial in tuning the optoelectronic properties of CDs toward a specific goal.

Herein, we report the first detailed investigation of the photophysical properties at both bulk-state and single-particle levels of CDs having electron acceptors and electron donors directly passivated on their nanoscale surface. It was interesting to note that even though the bulk-state experiments revealed that acceptor CDs were dominating the photophysical properties when mixed with donor CDs, it was not observed from our single-particle experiments. Bulk-state measurements refer to the ensemble-averaged measurements of the CDs (in aqueous solutions) wherein the observations of several features, such as photoluminescence, time-resolved photoluminescence (TRPL), 2D excitation and emission measurements (EEM), etc., are a result of the summations of their individual contributions.

2. Results and Discussion

In this work, we present a comprehensive investigation on the electron-donating as well as electron-accepting natures of CDs that have been passivated with malononitrile and N,N-dimethylaniline, which can behave as excited-state electron acceptors and electron donors, respectively. We first validated the electron donating/withdrawing capacity of malononitrile (electron acceptor) and N,N-dimethylaniline (electron donor) by calculating their electrostatic potentials as well as highest occupied molecular orbital (HOMO)–lowest unoccupied molecular orbital (LUMO) orbital energy diagrams via density functional theory (DFT) (**Figure 1**a,b). Electrostatic potential mapping displayed the availability of a lone-pair of electrons on N,N-dimethylaniline, with regions of negative electrostatic potential energy (red). As expected, malononitrile displayed a positive electrostatic potential energy (blue), thereby suggesting that it could behave as an electron acceptor. Results from DFT calculations corroborated this finding based on their HOMO–LUMO bandgap values. N,N-dimethylaniline has a higher ionization potential ($\Delta E_{i.p.} = -0.717$ eV), whereas malononitrile has a high electron affinity ($\Delta E_{e.a.} = 9.512$ eV), thereby making them perfect candidates for excited-state electron donors and electron acceptors, respectively (Figure 1b).

Using a hydrothermal synthesis route,[41] we prepared bare CDs (no surface passivation) with sucrose as a carbon source. CDs that were passivated with acceptor molecules (malononitrile) and donor molecules (N,N-dimethylaniline) will be referred as CD-A and CD-D, respectively, throughout the manuscript. Various combinations of sucrose and acceptor/donor small molecule (1:1, 1:2, and 1:5 w/w ratio) were used, and consequently termed as CD-A_1, CD-A_2, and CD-A_5 or CD-D_1, CD-D_2, and CD-D_5. These particles were subjected to purification by dialysis (infinite sink) against nanopore water (18.2 MΩ cm) using a cellulosic membrane (10 kDa molecular weight cut-off (MWCO)) with water replacement every 4 h, ultimately filtering it with 0.2 μm filter, followed by freeze-drying and redispersion in water.[42] Because the boiling points of both the acceptor and donor molecules are greater than 180 °C, we synthesized CDs at 180 °C for 12 h,[17] so that their structural integrity was not compromised during the hydrothermal synthesis. Mass spectrometric analysis was performed to confirm that both the donor and acceptor molecules survived the treatment (Spectrum S1 and Spectrum S2). Note that there is a possibility that during the nucleation of CDs, a few acceptor or donor small molecules could be trapped within the core. However, once the nucleation step has been completed, which is usually quick, the majority of these small molecules will be passivated onto the CD surface. This idea is supported by several experiments in the later section.

The purified nanoparticles were subjected to exhaustive physiochemical characterization prior to measuring their photophysical properties at the bulk level. We presented the results for CD-A_5 and CD-D_5 in the main manuscript and the rest CDs in the Supporting Information. Hydrodynamic diameter measurements were carried out using dynamic light scattering (DLS) (**Figure 2**a), which revealed their hydrodynamic diameter to be between 8 and 12 nm. The mixing of CD-A_5 and CD-D_5 in equal volume (CD-A_5 + CD-D_5) resulted in an increase in their hydrodynamic diameter to ≈40 nm (Figure 2a). The ζ-potential was negative for all CDs, less than −10 mV, indicating their colloidal stability (Figure 2a, inset). For bare CD, UV–Vis showed a typical π–π^* transition of the conjugated C=C bond at 280 nm (Figure 2b).[43] Surface decorated CD-D_5 and CD-A_5 revealed a similar π–π^* band, although it displayed a bathochromic shift (blue shift) and additional peak from 330–360 nm, which could be attributed to n–π^* transition.[44] We envisage that once

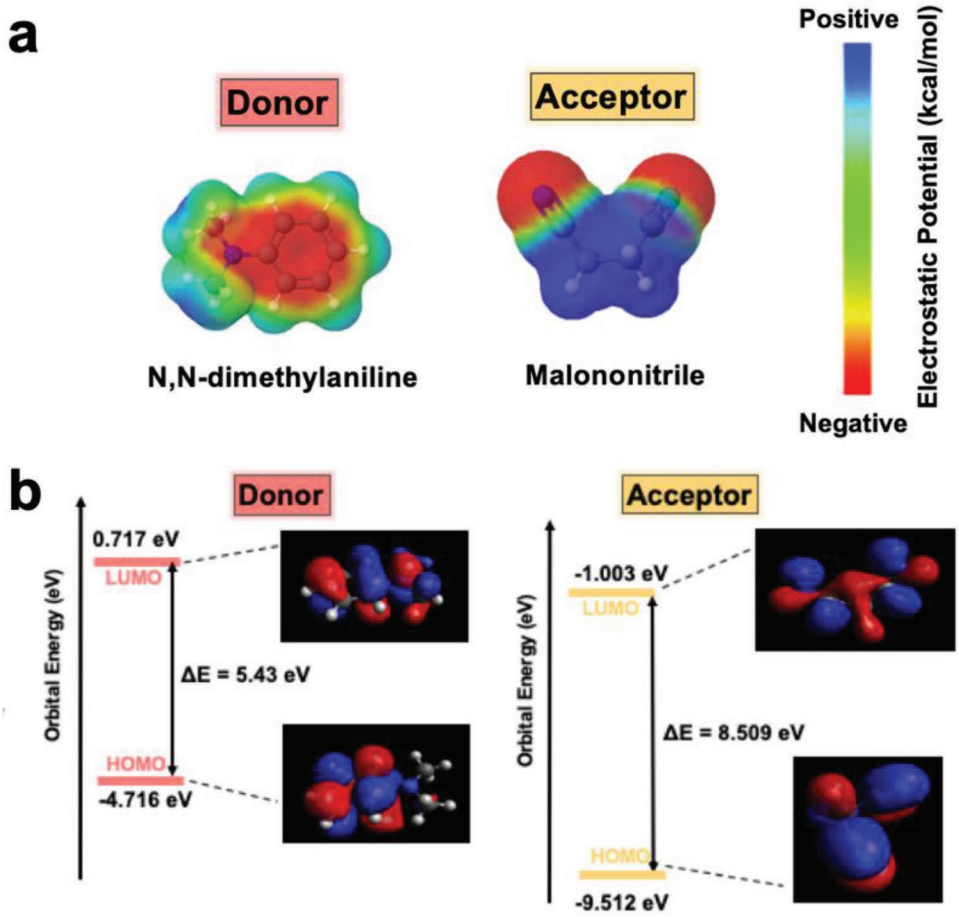

Figure 1. a) Molecular electrostatic potential maps of both N,N-dimethylaniline (donor) and malononitrile (acceptor) are shown to illustrate the charge distributions of molecules three-dimensionally, allowing us to visualize variable charge distributions of the molecule with a representative scale bar provided. b) DFT based calculations of molecular orbitals for HOMO and LUMO for both donor and acceptor have been highlighted, indicating their nature as electron donor and electron acceptor when taken together, respectively.

acceptor (A) or donor (D) molecules were passivated onto a CD surface, it led to electron- or charge-transfer between either of these molecules (A or D) and the surface groups on the CD surface (such as COOH, OH, etc.), resulting in the appearance of this peak between 330 and 360 nm. Interestingly, the maxima of the peaks for CD-D was 360 nm, whereas for CD-A it was 335 nm, indicating a possible electron- or charge-transfer process occurring between surface molecules of CDs with donor molecules (D) different from the acceptor molecules (A). Curiously, CD-A_5 + CD-D_5 mixture showed a UV–Vis absorption spectrum similar to that of CD-A_5, indicating that CD-A could dominate the absorption, and consequently their photophysical properties, in a mixture of CD-A and CD-D. A more thorough investigation of these electron or charge-transfer events was carried out in the later sections by performing more bulk-level photophysical experiments, utilizing DFT, and single-particle imaging experiments. All these samples were kept under UV lamp ($\lambda_{ex.}$ = 365 nm) and showed that bare CDs had green emission, albeit with low brightness (grey value). However, CD-D_5 and CD-A_5 both revealed a blue emission with the latter showing a sharper brightness. This was also quantified using ImageJ (Figure 2c), which revealed that bare CDs had the least brightness (grey value), followed by CD-D_5 (1.5-fold increase) and CD-A_5 (1.8-fold increase). Interestingly, CD-A_5 + CD-D_5 revealed a similar brightness (grey value) as CD-A_5 (1.8-fold increase). Next, to confirm if the increased brightness of CDs passivated with electron-accepting or electron-donating molecules resulted in enhanced photoluminescent quantum yields (QY), we calculated the QY values for all the CDs using quinine sulfate (Φ = 0.54) as a reference. It was observed that bare CDs had a quantum yield value of 0.13. CD-D_5 and CD-A_5 showed much higher QY values of 0.31 and 0.43, respectively. As expected, CD-A_5 + CD-D_5 had a similar QY value to CD-A_5 of 0.45 (Table S1, Supporting Information).

X-ray photoelectron spectroscopy (XPS) measurements were performed to elucidate the surface elemental mapping of all CDs (bare CDs, CD-D_5, CD-A_5, and CD-A_5 + CD-D_5). Bare CDs show C1s (284.6 eV) and O1s (532.5 eV) peaks (Figure S1, Supporting Information), whereas CD-D_5, CD-A_5, and CD-A_5 + CD-D_5 showed an additional N1s (400.0 eV) (Figures S2–S4, Supporting Information).[24] However, it was interesting to note that since CD-A_5 + CD-D_5 formed complex assembled structure, XPS measurements revealed their N% and O% intermediate of individual CD-D_5 and CD-A_5 particles. However,

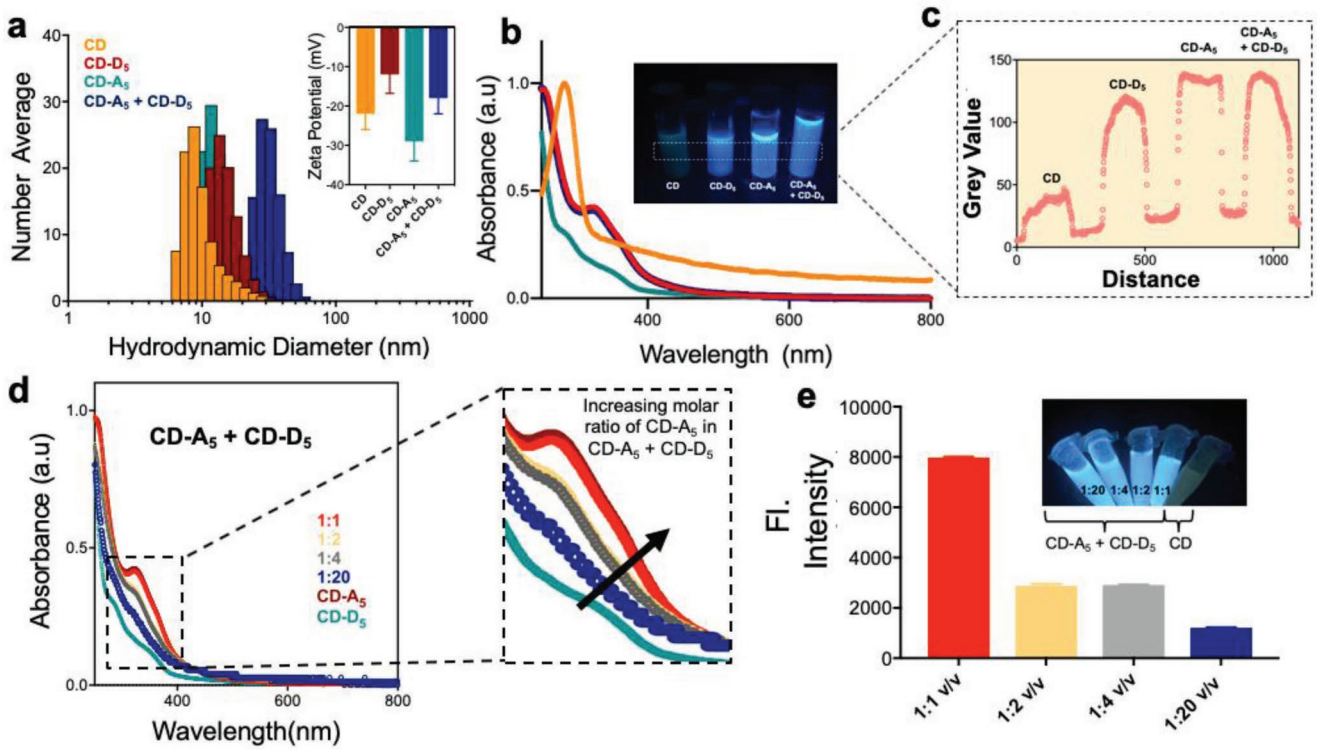

Figure 2. a) Hydrodynamic diameter distribution of CD, CD-D_5, CD-A_5, and CD-A_5 + CD-D_5 obtained via DLS. Inset: ζ-potential measurements of the CD samples. b) UV–Vis absorption spectra of CD, CD-D_5, CD-A_5, and CD-A_5 + CD-D_5. c) Inset includes these samples under UV light excitation of 365 nm and corresponding brightness profile (grey scale) has been calculated for each using ImageJ. d) Absorption spectra during the course of titration wherein increasing v/v ratio of CD-A_5 was added to CD-D_5 with UV–Vis absorption spectra of CD-A_5 and CD-D_5 alone have been provided for comparison. e) Corresponding fluorescence intensities of titrated samples (1:1 v/v, 1:2 v/v, 1:4 v/v, and 1:20 v/v) were collected at 500 nm emission ($\lambda_{ex.}$ = 400 nm). Inset: Different CD samples kept under UV light excitation of 365 nm.

an increase of C% when compared to individual particles could be simple indicative of additive contribution resulting from geometrical nonuniformity of the complex. To understand the bonding states of each element, high-resolution C1s, N1s, and O1s spectra were analyzed with a Gaussian fitting software, and the results obtained were shown in Figures S1–S3 (Supporting Information). The C1s band was able to deconvoluted into three peaks, corresponding to C=C/C−C (≈284.6 eV), C−O, C−N (≈286.5 eV), and C=O (≈288.3 eV).[45,46] However, for CD-D_5, one additional peak was obtained for COOH (≈289 eV). The O1s band contained two peaks at 531.7 and 533 eV for C=O and C−O, respectively.[47] The N1s band can be deconvoluted into three peaks, pyridinic N (≈399.6 eV), amino N (≈400.5 eV), and pyrrolic N (401.6 eV).[48] However, for CD-A_5, the pyrrolic peak was absent. The elemental composition of the CDs and a detailed analysis of O1s, C1s, and N1s of different CDs have been summarized in Tables S3–S6 (Supporting Information).

Steady-state absorption titration was performed to provide a more definitive confirmation about the dominance of CD-A_5 population on the photophysical properties of a CD-A_5 and CD-D_5 mixture as well as a potential electron- or charge-transfer occurring between them (Figure 2d,e; Figure S5, Supporting Information). The concentration of CD-D_5 was fixed, and CD-A_5 was added slowly in increasing amounts (v/v ratio increasing from 1:20 to 1:1), and the corresponding changes in the absorption spectra were recorded. It was observed that increasing the volume of CD-A_5 to CD-D_5 during the titration assay resulted in an increase in absorbance (Figure 2d) and the spectral nature gradually shifted from CD-D_5 alone to CD-A_5 alone. Consequently, these titrated samples were further visualized under the UV lamp (Figure 2e, inset) and their fluorescence intensity values at 500 nm were collected (excitation wavelength: 400 nm). Higher volume ratio of CD-A_5 in the CD-A_5 + CD-D_5 mixture resulted in an increased intensity and more brightness (Figure 2e). A similar trend was observed for other weight ratios (Figure S5, Supporting Information).

Transmission electron microscopy (TEM) was performed on different CD samples to probe their anhydrous state size and morphology (Figure S6, Supporting Information). Both CD-D_5 and CD-A_5 exhibited clear circular outlines without any severe aggregation, although from the particle size distribution analysis, the anhydrous diameters of CD-A_5 (11 ± 3 nm) were higher than CD-D_5 (3 ± 2 nm). However, from the DLS measurements, the hydrodynamic diameters were comparable and could potentially be due to different degrees of hydration-layer formation on these two CDs, which gets removed when they are evaporated and dried for TEM measurements. However, associated structure (as highlighted in Figure S6c, Supporting Information) formed in the CD-A_5 and CD-D_5 mixture, which could originate from the interaction between CD-A and CD-D nanodots. To determine both particle height and surface topography and to get a better resolution of the associated structures

formed when acceptor and donor CDs are mixed together, atomic force microscopy (AFM) measurements were carried out. These measurements were performed individually on CD-A_5 and CD-D_5 and revealed that they could be imaged as discrete particles. However, once they were mixed together, i.e., CD-A_5 + CD-D_5 (**Figure 3**a,b) or CD-A_1 + CD-D_1 (Figure S7c,d, Supporting Information), they tended to form a mixture of ring-like and rod-like structures, albeit it was much lower for the lower specific weight ratios (1:1) as compared to the higher specific weight ratios (1:5).

The observed ring-like or rod-like association is presumably an outcome of a process driven by the mutual association of donor–acceptor groups abundant on CD-D and CD-A nanodots, respectively. A schematic illustration of this proposed process is shown in Figure 3a leading to the hollow spherical structure. In this two-level structural hierarchy, initially we observed a simpler assembly process (rod-like morphology), which could serve as the building blocks in the course of the second stage to form the hollow ring structures (Figure 3b–d). We also briefly attempted to classify how the CDs would be constituted within a ring assembly by using ImageJ and found them to be constituted of alternating arrangements of CD-A_5 and CD-D_5 dots arranged in a ribbon-like manner (Figure S7, Supporting Information). However, in Figure 3d, we have kept the rings as single particle chains, since more proof is needed to confirm it is a ribbon-like arrangement, which is outside the scope of the current work. Height profile for the AFM image of ring-like structure was also performed with Gywddion, as shown in Figure 3d. Mechanistically, this observation can be explained by the electrostatic attraction between a group of CDs, which provides a stabilizing force as they come in close proximity and form a charge-transfer complex with associated "ring" structures, minimizing the electrostatic potential of the complex. As an alternate case, these mixtures of CDs have been also shown to form associated "rod" structures as highlighted but were found to be significantly lesser in number compared to the associated ring structures (Figure 3f). We attempted to provide an understanding of this by performing electrostatic potential calculations for conventional examples of a small rod (Figure 3h) or a hollow ring (Figure 3g), which would corroborate with our associated rod and associated ring structures obtained by association of CD-A_5 and CD-D_5 nanodots in the bulk. Based on that, we found that the value of electrostatic potential of an associated ring structure comes out to be smaller than that of an associated small rod structure (Supporting Information). We believe that lower value of the electrostatic potential stabilizes the charge transfer complex formed in the ring, and the rings are therefore more abundant in the AFM topography image, as clearly seen in Figure 3d. However, this is just conjecture, and further experiments will be needed to confirm this, which is outside the current scope of this work. We further performed additional experiments which demonstrated that the formation of these associated structures is dependent on several factors including time, specific weight ratios, intramolecular charge transfer, and hydrogen bonding (Figures S8–S10, Supporting Information). For showing that these associated structures are time-dependent, we performed TEM studies at t = 10 min after mixing and t = 1 month after mixing with the former showing

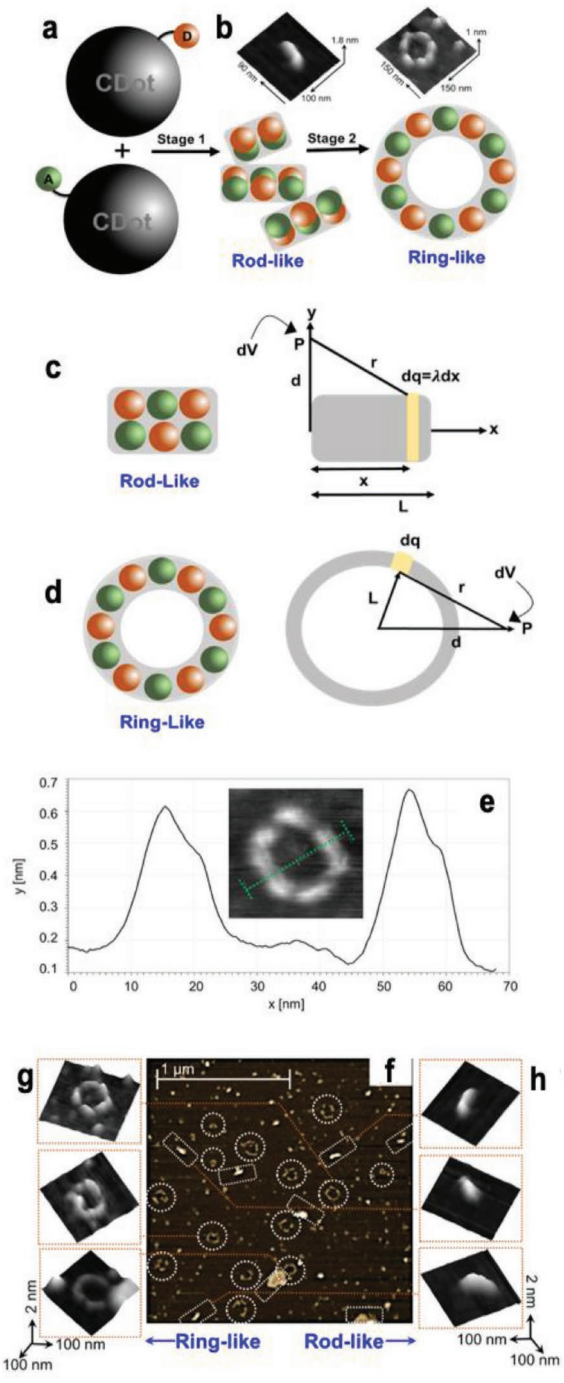

Figure 3. a) Schematic representation of CDs having electron acceptor or electron donors passivated on their surface and when mixed together could form a ring-like or associated rod-like structure. b) Subsequent atomic force microscopy (AFM) topographic images have been shown to indicate the ring-like and rod-like structures obtained. c,d) Representative rod-like and ring-like structures, respectively, along with parameters labeled which were involved in electrostatic potential calculations. e) Height profile for the AFM image of ring-like structure in the middle. f) AFM image taken when CD-D_5 and CD-A_5 were mixed together resulting in formation of two vivid structures—ring-like (highlighted in dotted circles) and rod-like (highlighted in dotted rectangles). Subsequent g) ring-like and h) rod-like structures have been highlighted, with ring-like structures being in more abundance.

associated rod-like structures, whereas the latter showing a combination of ring-like, rod-like, and other associated structures. We had previously performed AFM which revealed that CD-A_5 and CD-D_5 (sucrose: acceptor/donor small molecule: 1:5 w/w) mixed together showed a lot of associated structures as compared to CD-A_1 and CD-D_1 (sucrose: acceptor/donor small molecule: 1:1 w/w). In addition to this, we added electron quenchers (sodium chromate, SC) to the CD-A_5 and CD-D_5 mixture and collected both TEM and AFM images preaddition and postaddition. It was observed that the addition of SC resulted in the disappearance of the associated structures, with individual CDs (both CD-A and CD-Ds) dispersed throughout. This in turn means that the associated structures formed were due to an intramolecular electron transfer occurring between the surface of CD-A and CD-D nanoparticles. We further tried varying the pH of the system to acidic (pH 4 buffer and pH 2 buffer) and observed that breakage of the associated structures gradually. Hence, we believe that a combination of time, specific weight ratios, intramolecular charge/electron transfer, and hydrogen bonding is responsible for the formation of associated structures when CD-A and CD-D are mixed together.

First insights into the excited-state interactions came by performing the PL measurements at different excitation wavelengths (400, 450, and 500 nm). Here, we noticed that bare CDs had an emission maximum at around 530 nm with low intensity at 400 nm excitation. However, once either the acceptor molecules or donor molecules (at all the specific weight ratios, i.e., 1:1, 1:2, or 1:5) were passivated on the nanoscale surface of CDs, it resulted in the enhancement of the PL intensity accompanied by a blue-shift/bathochromic shift. Furthermore, when the w/w ratio of either acceptor or donor was increased to 2 or 5, a drop in PL intensity was observed, although it was still higher than that of bare CD (**Figure 4**a–c; Figures S11 and S12, Supporting Information). 2D EEM studies were also performed on these CDs, and it revealed that their emission centers highlighted with white arrows.

Next, TRPL emission profiles of different CD solutions were recorded at excitation wavelengths of 393 nm (**Figure 5**a) and 510 nm (Figure S13, Supporting Information), thereby ensuring a preferential excitation of the edge state of CDs as well as surface groups, respectively. Surface groups for bare CDs could be carboxylic acid groups, hydroxyl groups, etc., whereas for CD-D_5 or CD-A_5, surface groups would not only include the groups for bare CDs but will have donor and acceptor molecules passivated onto their surface, respectively. From the TRPL profiles for CDs at both excitation wavelengths (393 and 510 nm), it was evident that they demonstrated biexponential decay behavior.[49] The detailed fitting parameters have been listed in Table S2 (Supporting Information) and further explanation on the fitting process is discussed in detail in the Supporting Information. In Figure 5 and Figure S14 (Supporting Information), TRPL profiles for CD solutions at both $\lambda_{ex.}$ = 393 and 510 nm are shown. At $\lambda_{ex.}$ = 393 nm, average lifetime (τ_{avg}) of bare CD was ≈1.416 ns, whereas CD-D_5 and CD-A_5 showed an increase of average lifetime to ≈3.5 and 4.40 ns, respectively. However, when CD-D_5 and CD-A_5 were mixed together, the average lifetime increased to ≈4.6 ns, which was closer to the

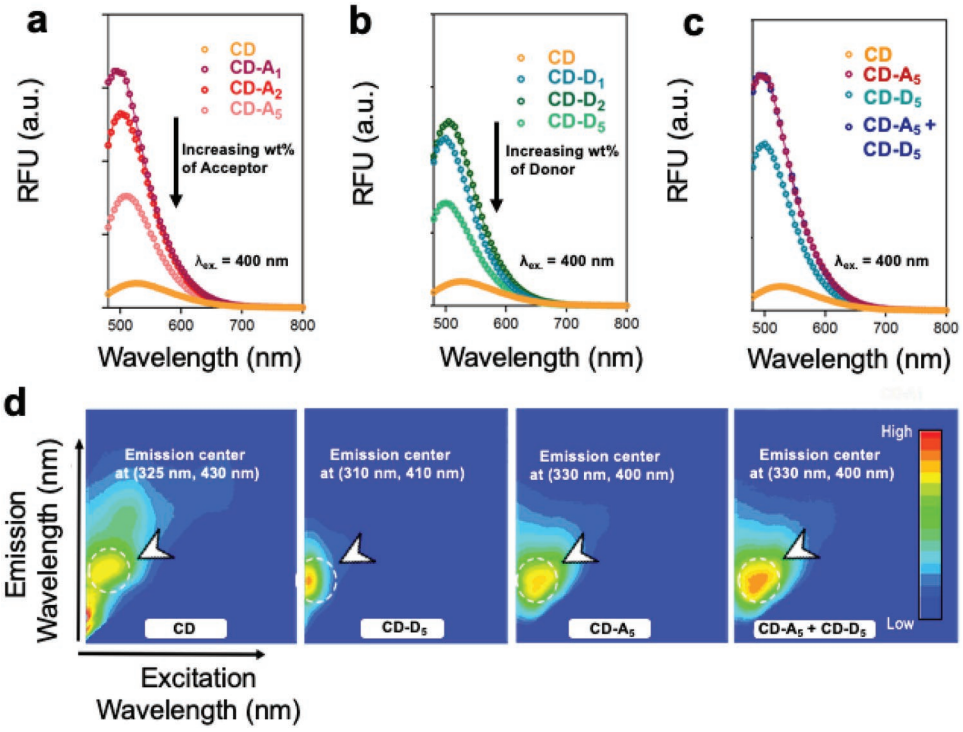

Figure 4. a) Photoluminescence (PL) emission spectra of CD-As with increasing w/w ratios of electron acceptor from 1:1 to 1:5. b) PL emission spectra of CD-Ds with increasing w/w ratios of electron donor from 1:1 to 1:5. c) PL emission spectra of CD-A_5 and CD-D_5 mixed together. Note that the excitation wavelength was 400 nm and PL emission spectra of CD (without passivation/surface modification) has been provided in each plot as a control. d) 2D excitation and emission (EEM) fluorescence images of CD, CD-D_5, CD-A_5, and CD-A_5 + CD-D_5 with their emission center highlighted with arrows.

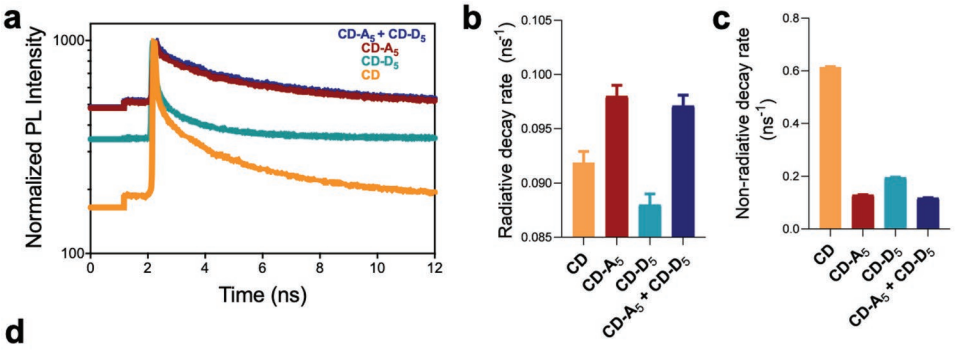

d

Sample	τ_1 (ns)	A_1 (%)	τ_2 (ns)	A_2 (%)	$\tau_{avg.}$ (ns)	χ^2	k_r (ns^{-1})	k_{nr} (ns^{-1})
CD	0.127	79.4	1.773	20.6	1.416	1.90	0.0919	0.615
CD-A_5	1.797	56.9	5.528	43.1	4.40	1.11	0.098	0.1295
CD-D_5	0.476	53.6	3.936	46.4	3.512	1.40	0.088	0.196
CD-A_5 + CD-D_5	1.26	40.9	5.201	59.1	4.632	1.17	0.0971	0.118

Figure 5. Time-resolved photoluminescence (TRPL) spectra of CD, CD-D_5, CD-A_5, and CD-A_5 + CD-D_5. b) Radiative and c) nonradiative decay rates for the CDs. d) Photophysical parameters of different CDs including intensity average lifetimes ($\tau_{avg.}$), radiative and nonradiative rates (k_r and k_{nr}). Excitation wavelength for TRPL experiments was kept to 393 nm.

average lifetime of CD-A_5, possibly indicating that the acceptor CDs dominate the photophysical properties when present in a mixture of CD-A and CD-D. It was interesting to note that the decay became faster for all CDs, once the excitation wavelength was increased from 393 to 510 nm, although the trend in the average lifetime of CDs was the same (Table S2, Supporting Information). Interestingly, the PL lifetime follows a similar trend to the PL QY across the different samples, i.e., CD, CD-A_5, CD-D_5, and CD-A_5 + CD-D_5. This close resemblance could possibly indicate that a disparity between the radiative and nonradiative recombination rates could be causing the difference between the above samples. Both these rates were calculated from the PL lifetime and PL QY results, by solving two equations simultaneously (Equations (1) and (2)), as done previously[50,51]

$$\tau_{avg.}^{-1} = \tau_r^{-1} + \tau_{nr}^{-1} \quad (1)$$

and

$$QY = \tau_{nr}/(\tau_r + \tau_{nr}) \quad (2)$$

where τ_{nr} stands for nonradiative recombination rate and τ_r stands for radiative recombination rate.

The radiative decay rate exhibited a similar trend to PL lifetime as well as the PL QY, i.e., higher for CD-A_5 compared to CD-D_5 and almost same for CD-A_5 + CD-D_5, whereas the nonradiative decay rate showed an inverse behavior wherein it was higher for CD-D_5 compared to both CD-A_5 or CD-A_5 + CD-D_5. For CD alone, the nonradiative decay rate was much higher when compared to other CDs (CD-A, CD-D, or CD-A + CD-D), thereby corroborating with its low QY (Figure 5b–d). To further elucidate the influence of these acceptor and donor molecules on the CD absorption and fluorescence properties, their electronic as well as emission properties were evaluated using DFT. We used an ovalene-based model, which was inspired from pyrene-based models that have been successfully applied as models in previous theoretical and experimental studies.[52] Relative comparison among different structures within the proposed model helped us in better understanding and explaining the photophysical properties of different CDs used in our experimental studies at both bulk level and single-particle level. For representing bare CDs, we constructed different ovalene-based structures having varying amounts of surface groups such as carboxylic acid groups and hydroxyl groups due to abundant percentages of carbon and oxygen as obtained from our XPS results (Table S3, Supporting Information). For representing CD-D_5 or CD-A_5, we constructed different ovalene-based structures having donor or acceptor molecules, respectively, on their surface along with carboxylic acid and hydroxyl groups (surface groups). Since CD-A_5 had more oxygen content as evident from XPS, the model was decorated with more surface groups as compared to CD-D_5 (**Figure 6**a–f). Following this, we performed DFT calculations on these small molecules, and to estimate which of the simulated structures closely represents a particular CD, we matched their bulk emission spectra with those of the emission spectra obtained for our simulated structures. Based on these rigorous DFT calculations, the calculated molecular orbital of LUMO and HOMO for CD-donor (CD-D_5) was placed higher than calculated molecular orbital of LUMO and HOMO of both CD and CD-acceptor (CD-A_5), thereby making it capable of donating electrons to either CD or CD-A_5 during the excited state or vice versa, i.e., either CD or CD-A_5 can act as excited-state electron acceptors when present together with CD-D_5. However, the HOMO and LUMO were placed higher for CD compared with CD-acceptor which would mean that CDs could behave as excited-state electron donors when present with CD-A_5 and vice versa, i.e., CD can

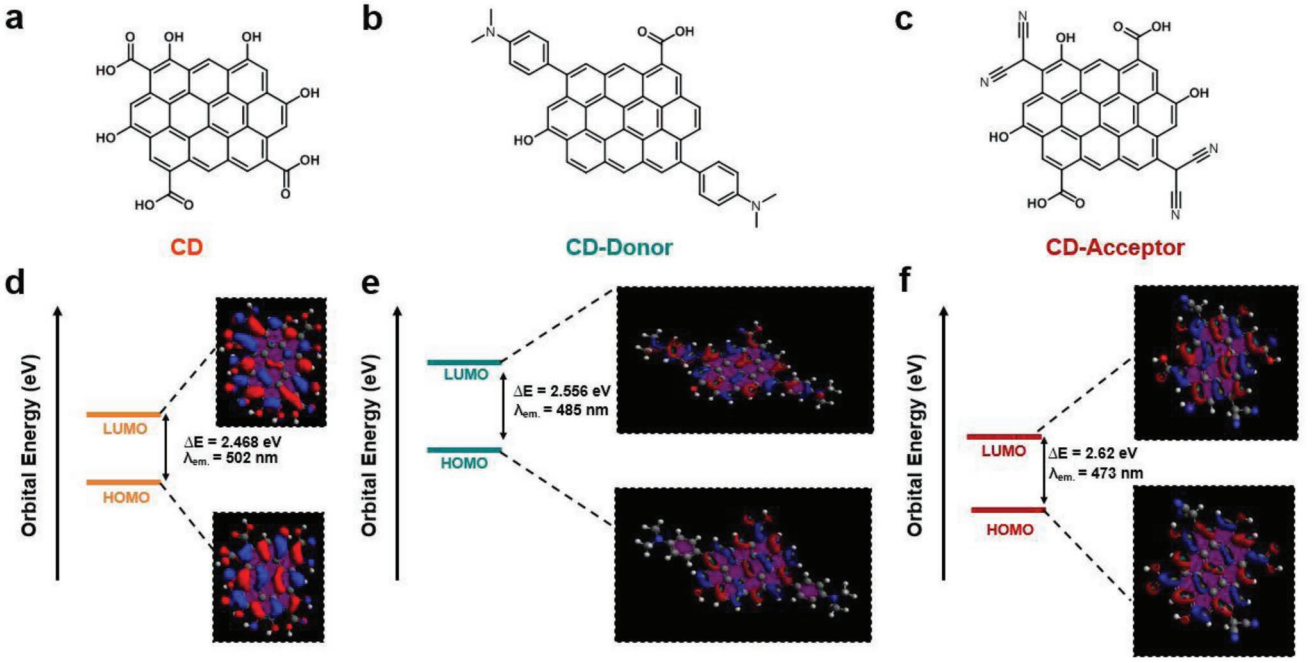

Figure 6. a) Ovalene-based structures was used to model CDs with representing a case of CD without any surface modification or bare CD, having functional groups (OH, COOH) obtained after nucleation. b) A case of CD-D wherein CDs were passivated with electron donors and c) represented a case of CD-A where CDs passivated with electron acceptors. d–f) Density functional theory (DFT) was performed on these model structures of CD, CD-D, and CD-A, respectively, so as to calculate the energy levels as well as HOMO and LUMO of the molecules.

act as an electron acceptor when present with CD. Hence, our elaborately designed theoretical calculations from DFT highlight that CDs could act as either electron-acceptors or electron-donors. At this point, we think it is important to point out that our theoretical calculations from DFT are based on simplistic modified models, which obviously do not take into account many experimentally relevant effects such as solvent or charged states. However, despite these shortcomings, our model was able to provide us a strong platform to explain our findings from our ensemble-average level and single-particle level experiments.

The observation that the CD-D_5 + CD-A_5 mixture behaved like CD-A_5 in the bulk analysis suggested a potential energy/electron transfer between CD-D_5 and CD-A_5 in the mixture. We hypothesized that this transfer depends on the direct association/interaction between CD-D_5 and CD-A_5. To begin to test this, samples were diluted to disrupt the particle–particle interaction to a distance (on average 1 µm between particles) that energy/electron transfer cannot occur. Individual particles were then analyzed using single particle imaging (SPI). We reasoned that analysis of photophysical properties by SPI would also allow us to better understand the observed enhancement of the quantum yield for CD-D_5 and CD-A_5 compared to CD.[53,54]

SPI resolved individual CD, CD-D_5, CD-A_5, and the CD-D_5 + CD-A_5 mixture as diffraction-limited spots (Figures S15–S19, Supporting Information). Within the 4 min data acquisition time (exposure time 100 ms), each sample showed single-step photobleaching with occasional recovery after initial bleaching (Figures S20 and S21, Supporting Information). First, we examined the instantaneous intensity (the average intensity of the emissive state) of CD, CD-D_5, CD-A_5, and the CD-D_5 + CD-A_5 mixture and found that there was an ≈10% increase in the instantaneous intensity for all samples compared to CD (**Figure 7**a,b). We then determined the on-time duty cycle for each sample and found that CD, CD-D_5, CD-A_5, and CD-D_5 + CD-A_5 mixture had a much higher on-time duty cycle compared to CD (Figure 7c,d). This result primarily arises from the increase in blinking frequency observed for CD-D_5 and CD-A_5 compared to CD (Figure 7e,f). To interpret this increase in blinking frequency, we determined the on-time and off-time distribution power law for all samples (**Figure 8**)

$$P\left(t_{\text{on/off}}\right) = At^{-\alpha} \tag{3}$$

$$\log\left(P\left(t_{\text{on/off}}\right)\right) = -\alpha * \log\left(t\right) + \log\left(A\right) \tag{4}$$

Overall, SPI analysis shows that the fluorescence intensity, photoblinking, and photobleaching observed for the CD-D_5 + CD-A_5 mixture is approximately the average of the results observed for the CD-D_5 and CD-A_5 samples (Figure 8d). This finding was in line with our hypothesis that the "acceptor-dominating" scenario observed in bulk measurements for the CD-D_5 + CD-A_5 mixture arises from direct particle interaction between CD-D_5 and CD-A_5.

To explain the change of on-time and off-time distribution, we use a model that describes the on and off states of a CD based on a previous model explaining the photoblinking

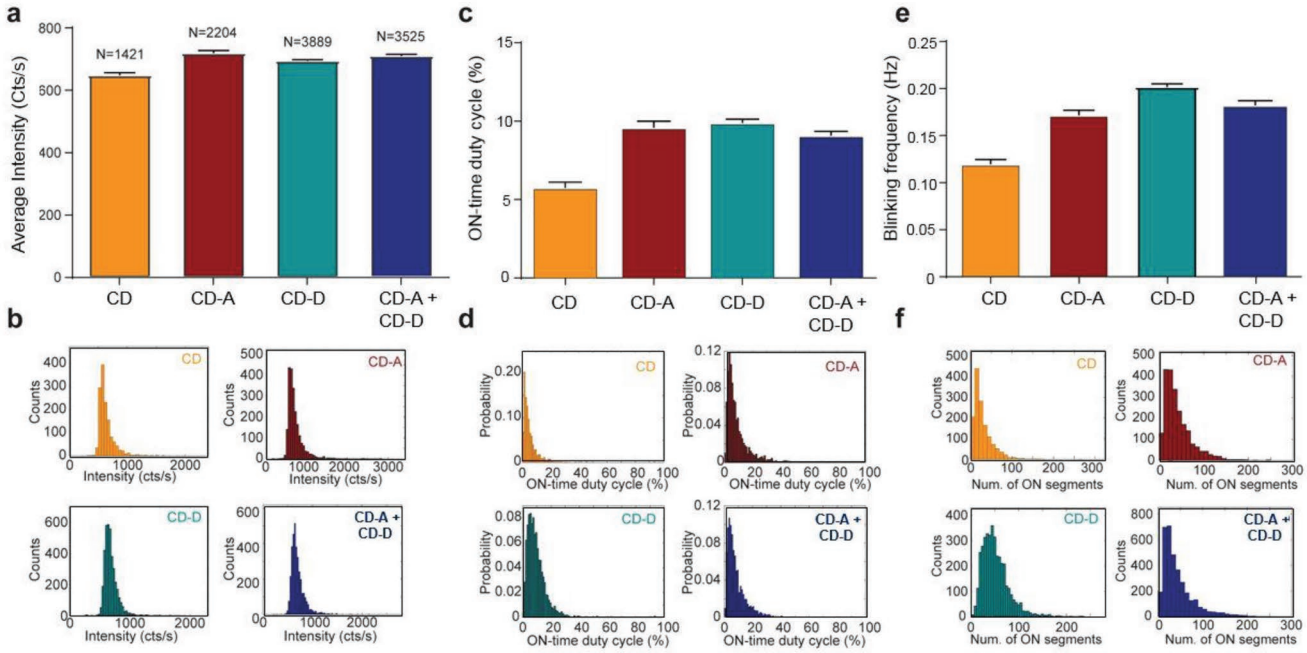

Figure 7. a,b) The average and distribution of single-particle instantaneous intensity, c,d) the ON-duty cycle, and e,f) the blinking frequency from the sample of CD, CD-A_5, CD-D_5, and CD-A_5 + CD-D_5 mixture. Error bars represent 95% confidence interval.

of carbon dots (**Figure 9**).[55] Upon excitation, a CD particle stays in its on-cycle as long as the electron stays in the fluorescent site (F) and the photostimulated electron decays back to the ground state, thereby emitting a photon (i, Figure 9). An on-cycle ends when the electron is transferred from F to a trap site (T) (ii, Figure 9). When an electron is recaptured by F, the off-cycle ends, and the next on-cycle starts (iii, Figure 9).

Any factor that accelerates the electron-recovery process by F results in a shorter off-time duration. For CD-A_5, once in an off-state (i.e., following electron transfer from F to T), we speculate that the electrophilic acceptor molecule (A) can grab an electron from T and become an apparent electron donor, which would increase the possibility of returning an electron to F (iv, Figure 9). This idea is supported by the observation that the off-time power-law slope increases from 1.36 for CD (Figure 8a) to 1.63 for CD-A_5 (Figure 8c), indicating a reduction of off-time duration.

In the case of donor molecules (D), we expect that electrons can be transferred to neighboring sites. In an on-state, spontaneous electron transfer from D to T (step 1 in v, Figure 9) in CD-D_5 converts the donor to an apparent electron acceptor, which then grabs an electron from F (step 2 in v, Figure 9), therefore shortening the on-time duration, as evidenced by a larger power-law slope, 2.32 (Figure 8b), in comparison to that of CD, 2.03 (Figure 8a). In an off-state, D in CD-D_5 acts as an additional electron source to replenish F (vi, Figure 9), therefore reducing the off-time duration, as indicated by a larger power-law slope, 1.77 (Figure 8b), in comparison to that of CD, 1.36 (Figure 8a).

As an immediate application of these CDs, we have shown that they could be used as a sensing array for metal ions and can serve as a powerful tool for the technological application of CDs by combining it with machine learning tools, e.g., linear discriminant analysis (LDA). The premise behind metal-sensing study of CDs is based on the charge-transfer process occurring between bare CDs (with surface groups such as COOH, OH, NH_2, etc.) and the metal ions. Since these charge-transfer processes will be different in our case where acceptor or donor small molecules have been passivated onto the CD surface (i.e., CD-A_5 or CD-D_5) or when they are mixed together (CD-A_5 + CD-D_5) resulting in associated structures, we tried using these four CDs in our study. We have demonstrated that we can utilize these CDs to develop an array for sensing metal ions in aqueous solutions (**Figure 10**a). In this direction, we measured the fluorescence emission for all the CDs in the presence of several types of metal ions at a concentration of 10×10^{-3} M. A higher quenching rate was observed toward Fe^{3+}, Cu^{2+} for CD-A_5 and the CD-A_5 + CD-D_5 mixture (Figure 10b). However, for Ru^{2+}, a high quenching rate was observed for all the CDs. A plausible reason could be that surface groups on the CD surface along with acceptor small molecules interact with the metal ions to form a coordination complex, facilitating annihilation of nonradiative electron/hole recombination and leading to electrons in the excited states transferring from the surface of CDs to the half-filled 3d orbital for Fe^{3+} ion.[27,56] By contrast, addition of other metal ions had no obvious quenching effect. We further analyzed the fluorescence data using LDA where two components were taken and plotted in a 2D graph from LDA values with 90% confidence ellipse (Figure 10c), and it shows clear separation of all the ions from each other. The Jacknified classification matrix (Table S7, Supporting Information) suggests 100% classification efficiency.

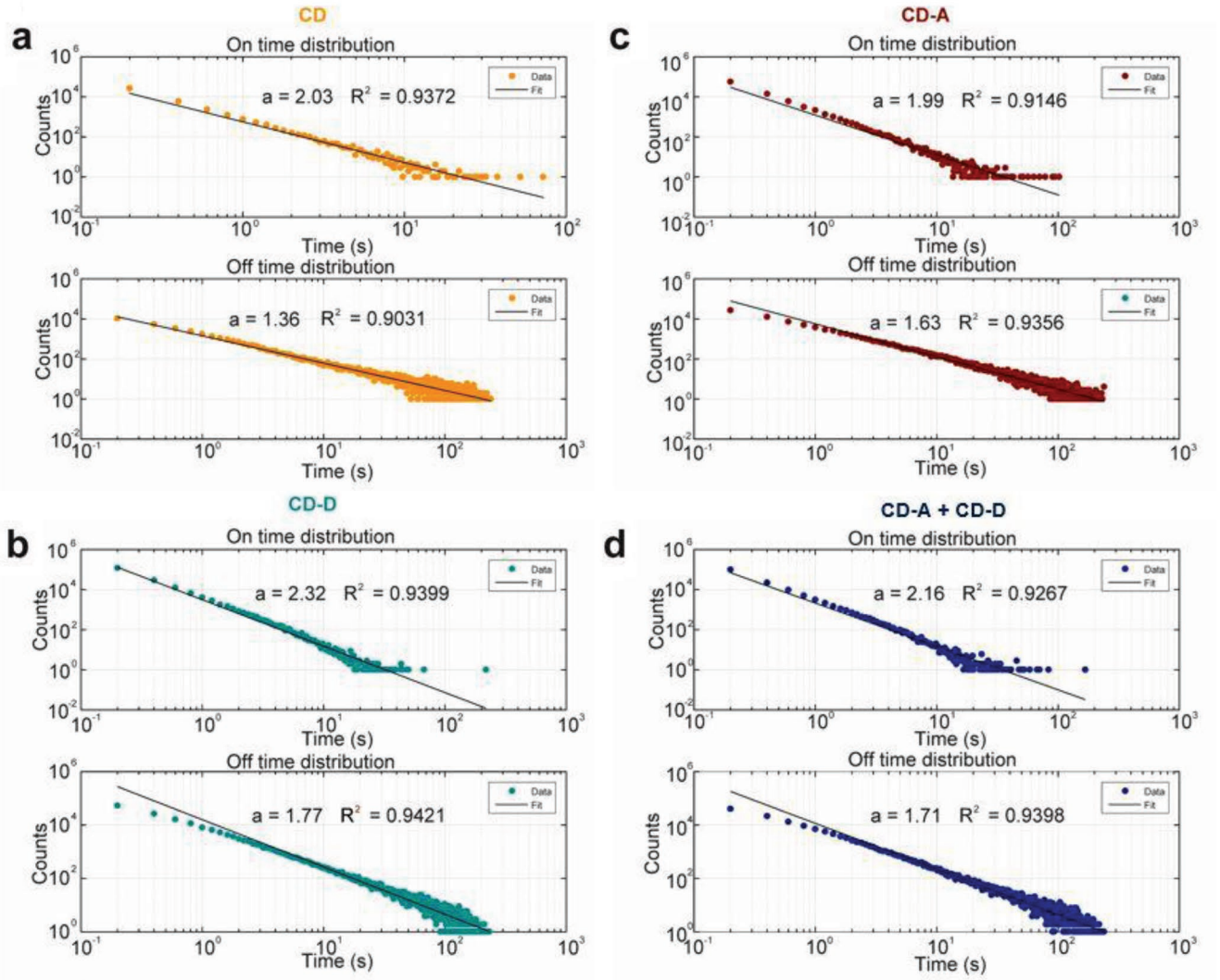

Figure 8. The power-law distribution of the on-time and off-time for a) pristine CD, b) CD-acceptor, c) CD-donor, and d) the mixture of CD-acceptor and CD-donor. The count and time duration (top: on, bottom: off) for each panel is plotted in a log–log scale. The slope of the time distribution was obtained by the fit results.

3. Conclusion

This study presents an in-depth investigation that proposes that CDs behave as simultaneous electron-acceptors and electron-donors at both the bulk state and single-particle level. To this end, we synthesized CDs passivated with electron-accepting and electron-donating groups on their surface and studied their photophysical properties. From our bulk-state experiments, we observed that CDs passivated with electron-accepting (CD-As) or electron-donating groups (CD-Ds) resulted in a blue-shift in emission along with a drastic increase in emission intensity, and consequently quantum yield. Interestingly, atomic force microscopy revealed that the mixing of donor and acceptor particles led to a formation of at least two associated geometries, displaying a two-level structural hierarchy. Bulk-state experiments with UV–Vis absorbance, time-resolved PL, EEM, and empirical studies with DFT indicated that acceptor populations (CD-A) dominate overall photophysical properties. Single-particle analysis revealed that the instantaneous intensity of CDs is comparable to that of CD-A_5, CD-D_5, and CD-A_5+ CD-D_5. However, CD-A_5 or CD-D_5 displayed larger on-time duty cycles, which was attributed to an increase of blinking frequency. On-time and off-time power-law analysis revealed that CD-A_5 has a larger off-time distribution slope than CD, whereas their on-time distribution was similar. On the other hand, CD-D_5 revealed an increase in both on-time and off-time distribution slope. These results indicate that the electron donor provides additional bright and dark states, but the electron acceptor primarily provides bright states. These additional states explained the increased blinking frequency in CD-A_5 and CD-D_5 at the single-particle level. Single-particle analysis, however, does not reveal an "acceptor-dominating" scenario based on analysis of instantaneous intensity, bleaching kinetics, and photoblinking, indicating that the direct interaction of CD-A_5 and CD-D_5 may affect their photophysical properties in the bulk due to formation of hierarchical structural assemblies.

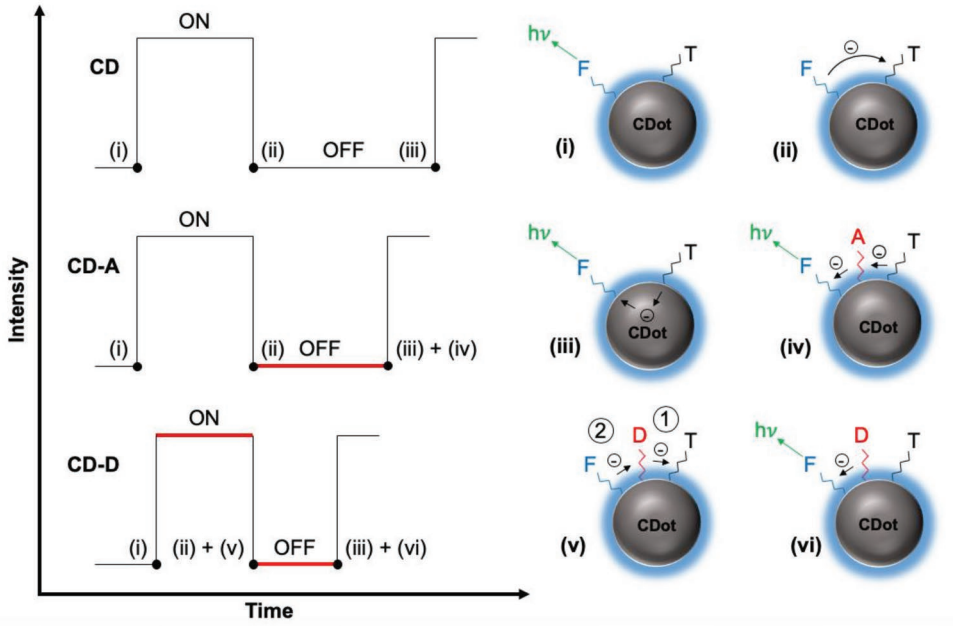

Figure 9. Proposed models for depicting the effect of donor and acceptor molecules on the on-time and off-time distributions of CD photoblinking. (i–vi) On–off transition points for single-particle fluorescence trajectories for CD, CD-A_5, and CD-D_5. The on-time begins upon photoexcitation of the fluorescent site, F (i). The on-time ends and the off-time begins at the moment of electron transfer from F to a trap site, T (ii). The off-time ends and the on-time begins again at the moment of electron transfer back to F (iii). The electrophilic acceptor molecules (A) in CD-A_5 facilitate the electron-recovery by F (iv), resulting in a reduction of off-time duration. Spontaneous electron transfer from donor molecules (D) to T (step 1 in v) in CD-D_5 results in an additional route for F to lose an electron (step 2 in v), and therefore a shortened on-time duration. Donor molecules in CD-D_5 also provide an additional electron source to replenish F (vi), therefore, reducing the off-time.

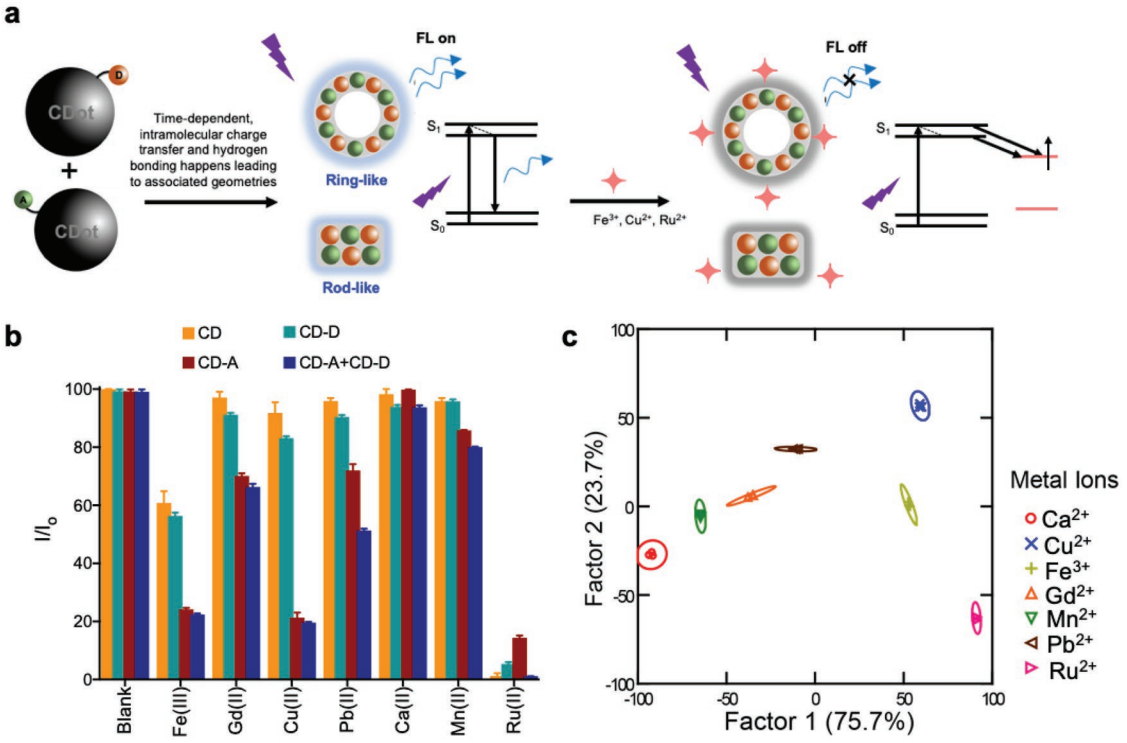

Figure 10. a) Schematic illustration of formation of associated structures when CD-A and CD-D are mixed together and can be used for the detection of metal ions, such as Fe^{3+}, Cu^{2+}, and Ru^{2+}. b) Relative fluorescence intensities of CD, CD-D_5, CD-A_5, and CD-A_5 + CD-D_5, where I and I_0 are the intensities in the presence and absence of the metal ions. c) Detection of seven metal ions using CD array where LDA was performed and shows clear differentiation of all the ions from each other.

We anticipate that these fundamental results will further enhance our understanding of the complex mechanism of CD emission, which is one of the key factors for their successful applications.

4. Experimental Section

Synthesis of CDs: The surface-modified carbon dots were prepared using sucrose as the carbon source, and an electron donor (N,N-dimethylaniline) or electron acceptor (malononitrile) as the surface passivating molecule. The carbon source and the electron acceptor/donor were combined in 20 mL glass vials in the following three weight ratios: 1:1 (50 mg sucrose, 50 mg donor/acceptor), 1:2 (50 mg sucrose, 100 mg donor/acceptor), and 1:5 (50 mg sucrose, 200 mg donor/acceptor). Samples of unmodified carbon nanodots will be referred to as CD, and acceptor-modified or donor-modified carbon nanoparticles will be referred to as CD-A or CD-D, respectively. One sample of unmodified nanoparticles using only sucrose was also prepared. Each sample was then combined with 5 mL of deionized (DI) water and vortexed until the solution appeared to be mixed well.

The nanoparticles were formed by hydrothermal synthesis by autoclaving all samples in enclosed reaction chambers at a temperature of 180 °C for ≈12 h. The samples were then probe sonicated using a microtip for 15 min (Q700, Qsonica Sonicators, CT, USA) (Amp: 1, On: 2 sec, Off: 1 sec) and filtered using a 0.22 µm syringe filter (Millex, Merck Millipore Ltd., County Cork, Ireland). A total of ten samples were synthesized; three samples each of acceptor-modified or donor-modified carbon nanoparticles at three weight ratios (1:1, 1:2, 1:5), one sample of unmodified "blank" carbon nanoparticles, and an additional three samples of equal amounts of CD-A mixed with CD-D at the varying weight ratios (i.e., CD-A 1:1 was mixed with CNP-D 1:1). The purpose of this was to determine if any interactions between the donor and acceptor molecules would occur and to report any subsequent effects on particle stability, size, or properties.

Dynamic Light Scattering: Hydrodynamic size distributions of the nanoparticles were determined through dynamic light scattering measurements on a Malvern Zetasizer ZS90 instrument (Malvern Instruments Ltd, United Kingdom) at a fixed angle of 90°. 50 µL of the particle suspension were mixed with 950 µL of nanopure water before running the samples in the DLS machine. A photomultiplier aperture of 400 nm was used, and the incident laser power was adjusted to obtain a photon counting rate between 200 and 300 kcps. Measurements for which the measured and calculated baselines of the intensity autocorrelation function were within 0.1% range were used for calculating the diameter. All measurements were performed in triplicates of thirteen consecutive measurements.

Transmission Electron Microscopy: TEM samples were prepared using a 1:10 dilution of the carbon dot samples with water. Briefly, 2 µL of carbon dot solution was added to 20 µL of millipore 0.22 µm filtered water. 2.5 µL of this solution was drop-casted onto a 300- to 400-mesh carbon-coated copper TEM grid (Ted Pella Inc). The samples were kept in ambient air for 2 min, after which excess moisture was wicked away using qualitative filter paper (Whatman). Dried grids were stored in sealed centrifuge tubes prior to imaging. Imaging was conducted with a JEOL 2100 Cryo TEM using an acceleration voltage of 200 kV. The reported images are representative images of structures observed in abundance at various locations on the TEM grids.

Atomic Force Microscopy: AFM samples were prepared by adding 2 µL of the CD-A + CD-D solution to 20 µL of DI water and drop-casted onto a freshly cleaved mica foil (Electron Microscopy Science, Muscovite Mica). The excess liquid was removed by tilting the foil onto a filter-paper (Whatman), leaving just a layer of liquid. Then the samples were dried overnight in vacuum before mounting it onto a magnetic stab using an adhesive tab (Ted Pella). Then the samples were imaged on an Asylum Cypher AFM using BS-Tap300Al tapping tips (BudgetSensors). The reported images are representative of the structure observed in plenty at various locations.

UV–Vis and Fluorescence Spectroscopy: UV–Vis measurements and steady-state titrations were performed on samples and collected on GENESYSTM 10S UV-Vis Spectrophotometer (Thermo Scientific, MA, USA). For these measurements, 2 µL of the nanoparticle solution was diluted with 998 µL of water. The UV–Vis spectra were collected over the 230–800 nm range. Fluorescence measurements were taken using an excitation wavelength of 400, 450, and 500 nm and a gain of 70, with a measured emission range of 430–850 nm. Sample volumes of 200 µL were used, and samples were not diluted for fluorescence measurements.

Quantum Yield Calculations: Quantum yield was calculated using the equation below, where Φ represents quantum yield, I corresponds to the integrated fluorescence intensity, A corresponds to the absorbance at 365 nm, and η corresponds to the refractive index of the solvent. Quinine sulfite (QS, $\Phi_{QS} = 0.54$) in H_2SO_4 ($\eta = 1.33$) was used as the reference for quantum yield calculations. Absorbance and integrated fluorescence intensity values are given in Table S1 (Supporting Information).

$$\phi = \phi_R \times \frac{I}{I_R} \times \frac{A_R}{A} \times \frac{\mu}{\mu_R} \tag{5}$$

Where ϕ is the quantum yield, I is the measured integrated emission intensity, μ is the refractive index, and A is the absorbance. The subscript R refers to the standard, Quinine sulfate.

X-Ray Photoelectron Spectroscopy: XPS samples were prepared by drop-casting 50 µL of CDs, on ≈0.5 cm × 0.5 cm glass slides, allowing them to dry in a vacuum oven overnight, and then repeating the process until 2 layers had been dropcasted. XPS spectra were collected with Al Kα (1486.6 eV) radiation and were analyzed using CasaXPS software.

Zeta Potential Measurements: 50 µL of CDs were diluted with 950 µL water for zeta potential measurements. Measurements were repeated three times for each nanoparticle type, with 10 or more runs conducted for each measurement.

Time-Resolved Photoluminescence Measurements: TRPL lifetime experiments were performed for CDs at an excitation wavelength of 393 nm and at 510 nm for CDs with emission ranges of 400–700 nm and 525–700 nm, respectively. A single-photon-counting setup at MRL, UIUC facility was used. The experiment was performed with the life-time of emitting states with single photon sensitivity and <1 ns temporal resolution at a temperature of 273 K. A particle concentration of 1 mg mL^{-1} was used for the experiment in a volume of 200 µL loaded in a quartz cuvette.

Further Investigations on Rod-Like and Ring-Like Structure formed for CD-A_5 + CD-D_5: For testing the effect of hydrogen bonding on the associated structures, CD-A_5 + CD-D_5 was suspended in pH2 and pH4 buffers for 24 h at 37 °C before performing TEM images. For evaluating the influence of electron quenchers and hole quenchers, 5 mg mL^{-1} solutions of both sodium chromate, SC (electron quencher) and sodium oxalate, SO (hole quenchers) were made and incubated with CD-A_5 + CD-D_5 for 24 h.[57] Following this, gel dock luminescence images were collected at 530 and 605 nm emissions, as well as fluorescence intensities at 360 nm excitation and 460 nm emission (Gain 50) for 2.5 h were collected. TEM images were also acquired before and after treatments with SC and SO.

DFT Calculations: For DFT calculations, the molecules were built using an open-source molecule builder, Avogadro. Becke 3-term correlation functional, Lee, Yang, and Parr exchange functional (B3LYP), which is a hybrid DFT method, was used for calculating the molecular orbital structures. 6–31G(d) was used as basis set for the calculations. Gaussian 09 was used for running the simulation. The output files were analyzed by Avogadro to obtain the energy level of the molecules and to calculate the shape of HOMO and LUMO of the compounds.

Single-Particle Photobleaching and Photoblinking Analysis: Samples for single-particle photobleaching were prepared following previous work.[53,54] Briefly, a droplet of 0.2 µL of CDs samples was applied to a clean coverslip and allowed to dry before being placed on a home-built TIRF microscope equipped with a 100× oil immersion objective.[41] The mean excitation power before the objective is 1.5 mW cm^{-2}. For each field of view, 1200 time-stamped images were taken with the exposure time of 200 ms per frame, which accounts for a total of 8 min of

trajectory. The number of CDs per frame was counted by a home-written MATLAB script. The net signal of CDs was calculated by subtracting background from the gross CD's signal for each frame. A MATLAB script was used to fit the normalized emission decaying curve with a two-component exponential function. The photobleaching lifetime was extracted from the fitted values.

Single-particle photoblinking was analyzed following a previous work.[53] Briefly, single-particle trajectories were segmented to define bright and dark states based on the changepoint analysis.[38,39] On states were defined as the mean of the darkest segment plus three times the standard deviation of that segment. The distribution of on-time and off-time was generated by histogram of duration of individual segments. The photoblinking frequency was calculated by normalizing the number of on–off transition events over the total acquisition time.

Metal Sensing: A 10×10^{-3} M aqueous solution of all the metals was prepared. An aqueous solution of 1 mg mL^{-1} of all CDs was prepared, and consequently 1 mL of metal solution and 1 mL of CDs were added and the fluorescence intensity was collected at 360 nm excitation and 460 emission. The control was prepared by adding 1 mL of water in place of the metal solution.

Supporting Information

Supporting Information is available from the Wiley Online Library or from the author.

Acknowledgements

D.P. conceived the project. I.S., D.P., and K.Z. designed the experiments and wrote the paper. I.S., X.H., A.C., S.P., P.F., J.S.K., and R.T.H. performed the experiments. I.S., K.Z., and J.S.K. performed the experimental data analysis. J.S.K. and S.P. co-second authored the work. D.P., K.Z., and S.N. supervised the research. The authors thank Frederick Seitz Materials Research lab, Roger Adams lab, and ISTC for analytical measurements. The authors thank John Scott for Fluorescence EEM measurements. University of Illinois at Urbana-Champaign, National Science Foundation and National Institute of Health are acknowledged for partially supporting this work.

Conflict of Interest

Prof. Dipanjan Pan is the founder/cofounder of three University based start-ups. None of these entities, however, supported this work.

Keywords

carbon dots, donor–acceptor charge transfer complexes, hierarchical particle assembly, single-particle fluorescence imaging

Received: March 25, 2019
Revised: May 21, 2019
Published online:

[1] Z. Lin, W. Xue, H. Chen, J. M. Lin, *Anal. Chem.* **2011**, *83*, 8245.
[2] Y. T. Zhang, L. Wang, H. C. Zhang, Y. Liu, H. Y. Wang, Z. H. Kang, S. T. Lee, *RSC Adv.* **2013**, *3*, 3733.
[3] L. Cao, S. Sahu, P. Anilkumar, C. E. Bunker, J. Xu, K. A. Fernando, P. Wang, E. A. Guliants, K. N. Tackett, Y. P. Sun, *J. Am. Chem. Soc.* **2011**, *133*, 4754.
[4] H. Li, X. He, Z. Kang, H. Huang, Y. Liu, J. Liu, S. Lian, C. H. Tsang, X. Yang, S. T. Lee, *Angew. Chem., Int. Ed.* **2010**, *49*, 4430.
[5] S. Zhuo, M. Shao, S. T. Lee, *ACS Nano* **2012**, *6*, 1059.
[6] F. Zhang, X. Feng, Y. Zhang, L. Yan, Y. Yang, X. Liu, *Nanoscale* **2016**, *8*, 8618.
[7] B. C. M. Martindale, G. A. M. Hutton, C. A. Caputo, E. Reisner, *J. Am. Chem. Soc.* **2015**, *137*, 6018.
[8] S. Cailotto, R. Mazzaro, F. Enrichi, A. Vomiero, M. Selva, E. Cattaruzza, D. Cristofori, E. Amadio, A. Perosa, *ACS Appl. Mater. Interfaces* **2018**, *10*, 40560.
[9] J. Shen, Y. Zhu, X. Yang, C. Li, *Chem. Commun.* **2012**, *48*, 3686.
[10] Y. Li, Y. Hu, Y. Zhao, G. Shi, L. Deng, Y. Hou, L. Qu, *Adv. Mater.* **2011**, *23*, 776.
[11] X. Yan, X. Cui, B. Li, L. S. Li, *Nano Lett.* **2010**, *10*, 1869.
[12] Y. P. Sun, B. Zhou, Y. Lin, W. Wang, K. A. Fernando, P. Pathak, M. J. Meziani, B. A. Harruff, X. Wang, H. Wang, P. G. Luo, H. Yang, M. E. Kose, B. Chen, L. M. Veca, S. Y. Xie, *J. Am. Chem. Soc.* **2006**, *128*, 7756.
[13] G. E. LeCroy, S. K. Sonkar, F. Yang, L. Monica Veca, P. Wang, K. N. Tackett II, J. J. Yu, E. Vasile, H. Qian, Y. Liu, P. Luo, Y. P. Sun, *ACS Nano* **2014**, *8*, 4522.
[14] S. K. Misra, F. Ostadhossein, E. Daza, E. V. Johnson, D. Pan, *Adv. Funct. Mater.* **2016**, *26*, 8031.
[15] X. Huang, F. Zhang, L. Zhu, K. Y. Choi, N. Guo, J. Guo, K. Tackett, P. Anilkumar, G. Liu, Q. Quan, H. S. Choi, G. Niu, Y. P. Sun, S. Lee, X. Chen, *ACS Nano* **2013**, *7*, 5684.
[16] S. K. Misra, I. Srivastava, I. Tripathi, E. Daza, F. Ostadhossein, D. Pan, *J. Am. Chem. Soc.* **2017**, *139*, 1746.
[17] I. Srivastava, S. K. Misra, I. Tripathi, A. S. Schwartz-Duval, D. Pan, *Adv. Biosyst.* **2018**, *2*, 1800009.
[18] F. Ostadhossein, L. Benig, I. Tripathi, S. K. Misra, D. Pan, *ACS Appl. Mater. Interfaces* **2018**, *10*, 19408.
[19] X. T. Zheng, A. Ananthanarayan, K. Q. Luo, P. Chen, *Small* **2015**, *11*, 1620.
[20] H. Li, Z. Kang, Y. Liu, S. T. Lee, *J. Mater. Chem.* **2012**, *22*, 24230.
[21] S. K. Misra, P. Mukherjee, H. H. Chang, S. Tiwari, M. Gryka, R. Bhargava, D. Pan, *Sci. Rep.* **2016**, *6*, 29229.
[22] K. Hola, M. Sudolska, S. Kalytchuk, D. Nachtigallova, A. L. Rogach, M. Otyepka, R. Zboril, *ACS Nano* **2017**, *11*, 12402.
[23] B. Zhi, Y. Cui, S. Wang, B. P. Frank, D. N. Williams, R. P. Brown, E. S. Melby, R. J. Hamers, Z. Rosenzweig, D. H. Fairbrother, G. Orr, C. L. Haynes, *ACS Nano* **2018**, *12*, 5741.
[24] H. Ding, S. B. Yu, J. S. Wei, H. M. Xiong, *ACS Nano* **2016**, *10*, 484.
[25] H. Ding, J. S. Wei, P. Zhang, Z. Y. Zhou, Q. Y. Gaom, H. M. Xiong, *Small* **2018**, *14*, 1800612.
[26] S. Zhu, Y. Song, X. Zhao, J. Shao, J. Zhang, B. Yang, *Nano Res.* **2015**, *8*, 355.
[27] L. Vallan, E. P. Urriolabeitia, F. Ruiperez, J. M. Matxain, R. Canton-Vitoria, N. Tagmatarchis, A. M. Benito, W. K. Maser, *J. Am. Chem. Soc.* **2018**, *140*, 12862.
[28] T. Scharl, A. Cadranel, P. Haines, V. Strauss, S. Bernhardt, S. Vela, C. Atienza, F. Grohn, N. Martin, D. M. Guldi, *Chem. Commun.* **2018**, *54*, 11642.
[29] D. M. Guldi, N. Martin, *J. Mater. Chem.* **2002**, *12*, 1978.
[30] G. Uyeda, J. C. Williams, M. Roman, T. A. Mattioli, J. P. Allen, *Biochemistry* **2010**, *49*, 1146.
[31] B. C. Polander, B. A. Barry, *J. Phys. Chem. Lett.* **2013**, *4*, 786.
[32] L. Sanchez, M. Nazario, D. M. Guldi, *Angew. Chem., Int. Ed.* **2005**, *44*, 5374.
[33] F. Arcudi, V. Strauss, L. Dordevic, A. Cadranel, D. M. Guldi, M. Prato, *Angew. Chem., Int. Ed.* **2017**, *56*, 12097.
[34] A. Ferrer-Ruiz, T. Schari, P. Haines, L. Rodriguez-Perez, A. Cadranel, M. A. Herranz, D. M. Guldi, N. Martin, *Angew. Chem., Int. Ed.* **2018**, *57*, 1001.
[35] V. Strauss, J. T. Margraf, T. Clark, D. M. Guldi, *Chem. Sci.* **2015**, *6*, 6878.

[36] V. Strauss, J. T. Margraf, K. Dirian, Z. Syrgiannis, M. Prato, C. Wessendorf, A. Hirsch, T. Clark, D. M. Guldi, *Angew. Chem., Int. Ed.* **2015**, *54*, 8292.
[37] L. Vallan, R. Canton-Vitoria, H. B. Gobeze, Y. Jang, R. Arenal, A. M. Benito, W. K. Maser, F. D'Souza, *J. Am. Chem. Soc.* **2018**, *140*, 13488.
[38] S. K. Das, Y. Liu, S. Yeom, D. Y. Kim, C. I. Richards, *Nano Lett.* **2014**, *14*, 620.
[39] M. Pelton, D. G. Grier, P. Guyou-Sionnest, *Appl. Phys. Lett.* **2004**, *85*, 819.
[40] X. Wen, P. Yu, Y. R. Toh, X. Hao, J. Tang, *Adv. Opt. Mater.* **2013**, *1*, 173.
[41] H. Ding, J. S. Wei, N. Zhong, Q. Y. Gao, H. M. Xiong, *Langmuir* **2017**, *33*, 12635.
[42] D. Pan, J. L. Turner, K. L. Wooley, *Chem. Commun.* **2003**, 2400.
[43] S. K. Misra, H. H. Chang, P. Mukherjee, S. Tiwari, A. Ohoka, D. Pan, *Sci. Rep.* **2015**, *5*, 14986.
[44] F. Ostadhossein, G. Vulugundam, S. K. Misra, I. Srivastava, D. Pan, *Bioconjugate Chem.* **2018**, *29*, 3913.
[45] D. Qu, M. Zheng, L. Zhang, H. Zhao, Z. Xie, X. Jing, R. E. Haddad, H. Fan, Z. Sun, *Sci. Rep.* **2015**, *4*, 5294.
[46] J. Mondal, S. K. Srivastava, *ChemistrySelect* **2018**, *3*, 8444.
[47] K. Jiang, S. Sun, L. Zhang, Y. Lu, A. Wu, C. Cai, H. Lin, *Angew. Chem., Int. Ed.* **2015**, *54*, 5360.
[48] I. Tripathi, S. K. Misra, F. Ostadhossein, I. Srivastava, D. Pan, *ACS Appl. Mater. Interfaces* **2018**, *10*, 37886.
[49] J. H. Bang, P. V. Kamat, *ACS Nano* **2009**, *3*, 1467.
[50] S. Varghese, S. K. Park, S. Casado, R. Resel, R. Wannemacher, L. Luer, S. Y. Park, J. Gierschner, *Adv. Funct. Mater.* **2016**, *26*, 2349.
[51] S. Bhattacharya, F. Ehrat, P. Urban, R. Teves, R. Wyrwich, M. Doblinger, J. Feldmann, A. S. Urbana, J. K. Stolarczyk, *Nat. Commun.* **2017**, *8*, 1401.
[52] M. Shamsipur, A. Barati, A. A. Taherpour, M. Jamshidi, *J. Phys. Chem. Lett.* **2018**, *9*, 4189.
[53] S. K. Misra, I. Srivastava, J. S. Khamo, V. V. Krishnamurthy, D. Sar, A. S. Schwartz-Duval, J. A. N. T. Soares, K. Zhang, D. Pan, *Nanoscale* **2018**, *10*, 18510.
[54] P. Fathi, J. S. Khamo, X. Huang, I. Srivastava, M. B. Esch, K. Zhang, D. Pan, *Carbon* **2019**, *145*, 572.
[55] S. Khan, W. Li, N. Karedia, J. Thiart, I. Gregor, A. M. Chizhik, J. Enderlein, C. K. Nandi, A. I. Chizhik, *J. Phys. Chem. Lett.* **2017**, *8*, 5751.
[56] P. Lv, Y. Yao, H. Zhou, J. Zhang, Z. Pang, K. Ao, Y. Cai, Q. Wei, *Nanotechnology* **2017**, *28*, 1665502.
[57] S. Karunakaran, S. Pandit, B. Bas, M. De, *J. Am. Chem. Soc.* **2018**, *140*, 12634.